Pramana – J. Phys. (2024) 98:142
https://doi.org/10.1007/s12043-024-02839-7

Crystallisation of liquid silica under compression: a molecular dynamics simulation

VAN HONG NGUYEN[1,*] and HOANG ANH NGUYEN[2]

[1]Faculty of Engineering Physics, Hanoi University of Science and Technology, Hanoi 100000, Vietnam
[2]Colorado School of Mines, Golden, CO 80401, USA
*Corresponding author. E-mail: hong.nguyenvan@hust.edu.vn

MS received 17 May 2024; revised 28 July 2024; accepted 2 August 2024

Abstract. In this study, we employ molecular dynamics simulations to develop a large model (19,998 atoms) of liquid SiO_2 at 3500 K. We construct models at different pressures in the 0–100 GPa range using the Beest–Kramer–Santen (BKS) potential and periodic boundary conditions. The goal is to detail the structural transition from the polyamorphic liquid state of SiO_2 to the crystalline stishovite form, which occurs between 45 and 60 GPa. We analyse the polyamorphic state of liquid SiO_2 by examining the formation of SiO_x clusters from 2 to 60 GPa. Beyond 60 GPa, the pair radial distribution functions (PRDFs) for Si–O, O–O and Si–Si display multiple peaks, indicating the crystalline phase. This observation is further supported by examining the bond angle distribution, the fraction of SiO_x units and OSi_x linkages, Si–O bond lengths within SiO_x units, structural visualisations and the analysis of ring statistics in the liquid SiO_2 system, all of which underscore the comprehensive changes in the structure of the system.

Keywords. Liquid SiO_2; stishovite; SiO_2; ring statistics; polyamorphism; crystallisation.

PACS Nos **61.30; 61.10; 61.43.Fs**

1. Introduction

In recent decades, glass and liquid silica (SiO_2) have garnered significant attention from researchers due to their diverse applications in engineering materials and their relevance in earth sciences [1–7]. Grasping the densification mechanisms within this material is essential for addressing questions related to crystallisation, the development of ceramics with enhanced toughness and the composition of the Earth's upper and lower mantle boundaries [8,9]. Molecular dynamics simulations (MDS) are used to explore the equilibrium interface between the high-density liquid (HDL) and low-density liquid (LDL) phases of silica [10]. The investigation reveals a transition from fragile to strong dynamics across the silica HDL–LDL interface. Dynamic property analysis uncovers three distinct types of dynamical heterogeneity merging at this interface. Furthermore, crossing from the HDL to the LDL side significantly increases the Si/O coordination number ratio, marking a narrow zone where there is considerable mixing between the HDL and LDL phases. During compression, liquid SiO_2 simultaneously harbours both low-density and high-density phases. The scale of these phase regions is notably affected by the degree of compression applied [11]. The polymorphic phenomenon of liquid systems under compression is not exclusive to silica; other compounds like beryllium fluoride (BeF_2) [12], germania (GeO_2) [12–14], alumina (Al_2O_3) [15], boron trioxide (B_2O_3) [16], the mixture of yttrium oxide and aluminum oxide (Y_2O_3–Al_2O_3) [17], etc. also exhibit this behaviour. Besides MDS, the *ab-initio* method is an extensively applied tool to analyse microstructural evolution during solidification and structural phase transformations [18–21].

Despite numerous investigations into the crystallisation of glass SiO_2 and the polyamorphism of liquid SiO_2, the detailed mechanism underlying the structural phase transition from the polyamorphic state of liquid SiO_2 to crystalline stishovite SiO_2 has not yet been clarified. Especially, the ring statistics of liquid SiO_2 are still in question. This study aims to shed light on the complex transition. Furthermore, by employing MDSs, we have developed a liquid SiO_2 model comprising an expansive atomic ensemble of 19,998 atoms. This substantial

Published online: 10 October 2024

increase in the number of atoms allows for a more refined and higher quality research model than those limited to only a few thousand atoms, enhancing our ability to discern the intricacies of the structural phase transitions in SiO_2.

2. Methodology

In this work, the MDS is conducted on a model consisting of 19,998 atoms, out of which 6,666 atoms are Si and 13,332 atoms are O, utilising the Beest–Kramer–Santen (BKS) potential and periodic boundary condition. This potential is extensively applied to examine silica in both liquid and glass states [22–25]. Details regarding the BKS potential utilised can be found in [26]. In this study, the Verlet algorithm is employed with a time-step of 0.48 fs. The process begins with a random distribution of particles within the simulation box, which is subsequently heated to 6000 K to eliminate the initial configuration (to ensure that the model does not depend on the initial configuration). Following this, the system is sequentially cooled at a cooling rate of 2.5 K/ps to temperatures of 5000, 4500 and 4000 K with relaxation at each temperature stage and eventually, to 3500 K. When reaching the final temperature of 3500 K, the system undergoes an extended relaxation phase for 10^7 MD time-steps within the NPT ensemble, resulting in the formation of the liquid SiO_2 model in an equilibrium state at ambient pressure (0 GPa). The model is then compressed to achieve the desired pressures from 0 to 100 GPa. Each model is analysed by averaging the data collected from the last 1000 MD steps. For structural analysis, calculations are made for Si–O, O–O and Si–Si bond length distributions, Si–O–Si and O–Si–O bond angle distributions, the proportions of SiO_x units and OSi_x linkages, SiO_x cluster formation, formation of edge- and face-sharing linkages and the statistics of ring structures under varying pressures.

3. Results and discussion

3.1 *The bond lengths of Si–O, O–O and Si–Si under compression*

To understand the structural phase transition during the compression process, this study focusses on the local structure of the –Si–O– network, the short-range order (SRO) and the intermediate-range order (IRO) under compression. Figure 1 illustrates the variations in the pair radial distribution functions (PRDFs) of Si–O, O–O and Si–Si as pressure is applied. The IRO is analysed based on the formula $2\pi/Q$ where Q is the position of the first sharp diffraction peak [27]. At ambient pressure, the first peaks of the Si–O, O–O and Si–Si PRDFs are found at 1.60, 2.63 and 3.11 Å, respectively, aligning well with the findings from prior research [22,28–30]. As pressure escalates, the first peak of the Si–O PRDF remains relatively stable in position (i.e., location of the first peak remains relatively stable), yet its height diminishes and the full-width at half-maximum (FWHM) expands, indicating a reduction in SRO.

Above 60 GPa, the presence of multiple peaks in the PRDFs for Si–O, O–O and Si–Si suggests a phase transition from the polyamorphic state [15] of initial liquid SiO_2 to a crystalline phase. As pressure increases, the first peak in the O–O PRDF shifts to the left continuously, while the first peak in the Si–Si PRDF splits into two distinct sub-peaks starting at 60 GPa. This division in the Si–Si PRDF can be attributed to the emergence of edge-sharing and face-sharing bonds under high pressure (see table 1), alongside changes in the Si–O–Si angle distribution caused by the formation of OSi_3 units. As both liquid and glass SiO_2 exhibit a random, continuous network characteristic of polyamorphism, the transition from liquid SiO_2 to glass SiO_2 with increasing pressure is not delineated by changes in the PRDFs for Si–O, Si–Si and O–O. However, during crystallisation, the IRO of the crystal network markedly diverges from the continuous random network, enabling the identification of the crystallisation phase between 45 and 60 GPa in liquid SiO_2. The emergence of numerous peaks in the PRDFs of SiO_2 also aids in elucidating the

Table 1. Distribution of the number of bonds per one Si^{4+} ion. N_c is the number of corner-sharing bonds, N_e is the number of edge-sharing bonds and N_f is the number of face-sharing bonds

Pressure (GPa)	N_c	N_e	N_f
0	2.01	0.02	0.00
2	2.13	0.08	0.00
5	2.28	0.19	0.01
7	2.40	0.26	0.01
10	2.50	0.37	0.02
15	2.68	0.54	0.03
20	2.86	0.63	0.05
25	2.96	0.73	0.04
30	3.03	0.82	0.06
45	3.21	1.00	0.08
60	3.83	1.04	0.02
80	3.93	1.02	0.01
100	3.87	1.07	0.02

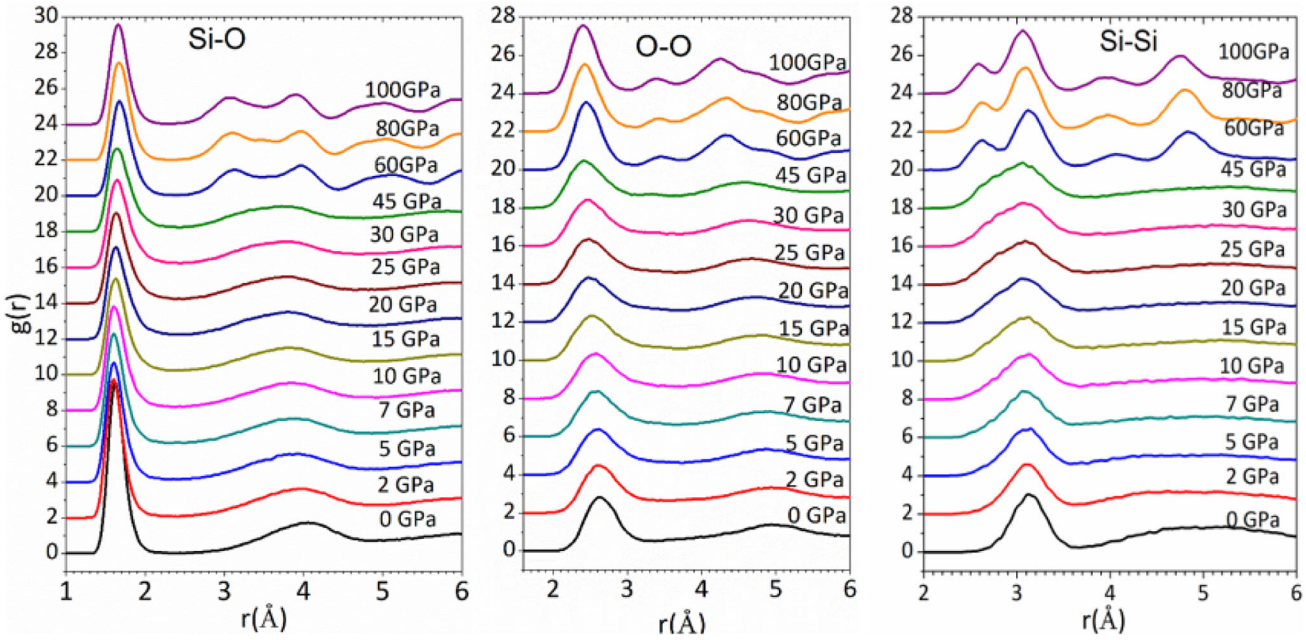

Figure 1. PRDF of Si–O, O–O and Si–Si at different pressures.

crystallisation process of glass SiO_2, though for glass SiO_2, crystallisation occurs under significantly lower pressures which is below 35 GPa [31–34].

Figure 2 presents a comprehensive analysis of the pressure-dependent variations in the number of SiO_x ($x = 4, 5, 6$) fundamental units and OSi_x ($x = 2, 3, 4$) linkages. At ambient conditions, the system predominantly comprises SiO_4 tetrahedral units, which tend to form networks mainly *via* bridging oxygen atoms which are associated with the OSi_2 linkages. By applying pressure, a remarkable transition occurs within this network. The SiO_4 units, initially the majority species, experience a substantial decline in their relative fraction while the fraction of SiO_5 and SiO_6 units increase. In the case of SiO_5, the fraction reaches the maximum value of about 50% at 15–20 GPa, followed by a strong decrease. At 100 GPa, SiO_5 units are virtually absent from the system. Conversely, the fraction of SiO_4 units exclusively decreases and the fraction of SiO_6 units exclusively increases. The trends of SiO_4 and SiO_6 are mirrored in the behaviours of OSi_2 and OSi_4 linkages, respectively, whereas OSi_3 linkages consistently remain below 5% throughout the entire pressure range. The pronounced change in the gradients of SiO_4, SiO_5, SiO_6, OSi_2 and OSi_4 at 60 GPa is indicative of a significant structural transformation occurring within the system at this pressure threshold.

Insights into the structure of SiO_x are also derived by analysing bond angle distributions in O–Si–O and Si–O–Si. These angles illuminate the internal atomic arrangement and the inter-unit connectivity within SiO_x, respectively. Bond angle distributions under compression in SiO_4, SiO_5 and SiO_6 units are detailed in figure 3. At ambient pressure, the SiO_4 units have a peak of 109°, which is close to the value of 107 ± 2° [22,26]. In SiO_2 glass, these values are in the range 109.5–109.7° [35–39]. The observation shows that the O–Si–O angle in ideal SiO_4 tetrahedra forms an ideal tetrahedrally bonded random network. At higher pressure, the bond angle distribution slightly shifts to the left, indicating that the tetrahedra distorts due to tension. For SiO_5 and SiO_6, the angle distributions peak at around 90°. However, in SiO_6, there is another peak at around 167°, suggesting distinct structural characteristics. Under compression, the O–Si–O angle distribution of SiO_4 slightly shifts to the left, reaching the value of around 105° at 30 GPa. The O–Si–O angle distribution of SiO_5 remains unchanged at different pressures. In SiO_6, two peaks are more pronounced from 60 GPa than their shapes at low pressures and the FWHM is narrower. Along with the PRDF distribution of Si–O, Si–Si and O–O (see figure 1), the system at 60 GPa primarily consists of SiO_6 (see figure 2).

When the structural transitions of liquid SiO_2 under different pressures are explored, particularly through the lens of Si–O–Si bond angles within the OSi_x linkages ($x = 2, 3, 4$) as depicted in figure 2b, we observe a nuanced interplay between pressure, bond angle distribution and structural transformation. At ambient pressure, the distribution of Si–O–Si in OSi_2 linkages manifests Si–O–Si bond angles around 145°, which is in good agreement

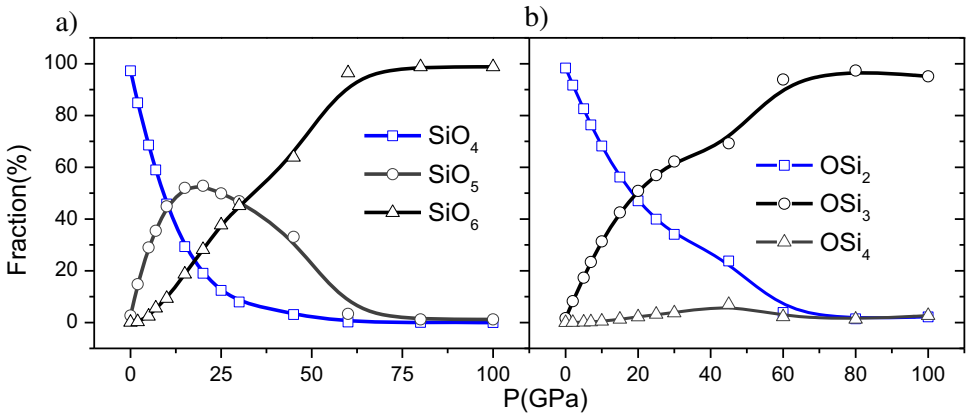

Figure 2. The fraction of SiO_x ($x = 4, 5, 6$) units (**a**) and OSi_x ($x = 2, 3, 4$) linkages (**b**) at different pressures.

with the previous work [22]. This configuration undergoes a small shift towards 140° at 30 GPa, hinting at the initial stages of structural rearrangement. Contrastingly, the Si–O–Si bond angle distributions of OSi_3 and OSi_4 linkages at similar pressures present a broader spectrum. The absence of a definitive peak in OSi_3 linkages suggests the transition towards more complex geometries that bridge tetrahedral and higher-coordinated structures. OSi_4 linkages, with a notable peak near 100°, signal a significant emergence of six-fold coordinated SiO_6. The transition observed at pressures exceeding 60 GPa, marked by the shift from a singular to dual peak distribution in Si–O-Si bond angles at 100° and 131° for OSi_3 and OSi_4 linkages, underscores a significant reconfiguration of the SiO_2 molecular network. The reduction in the Si–O–Si bond angles contributes to shorter Si–Si bond lengths, which in turn increases the Coulomb repulsion force [26] between the two Si atoms [34]. This escalation in repulsive forces leads to an elongation of Si–O bond lengths. Consequently, the Si–O–Si bond angle distribution's dual peaks in OSi_3 and OSi_4 lead to the splitting of the first peek of Si–Si PRDF into two different sub-peaks (see figure 1).

At ambient pressure, the liquid SiO_2 consists of SiO_4 units connected to others by corner-sharing bonds. When pressure increases, the edge-sharing and face-sharing bonds appear (see table 1) and contribute to form the –Si–O– network and the relative fractions of those bonds also depend on pressure. At pressures exceeding 60 GPa, the first peak of the Si–Si PRDF split into two distinct sub-peaks, located at 2.59 Å and 3.05 Å, as depicted in figure 1. This is attributed to the emergence of edge- and face-sharing bonds under high-pressure conditions. The interplay between the average bond lengths of edge- and face-sharing linkages and the splitting of the first peak is corroborated by many works, ranging from SiO_2 [40] to GeO_2 [41] and other various SiO_2-based materials [42–44]. Figure 4 illustrates the bond length distribution across the three types of bonds. At 100 GPa, the mean bond lengths of corner-sharing, edge-sharing and face-sharing bonds are determined to be 3.12, 2.72 and 2.53 Å, respectively. These measurements reveal a direct correlation between bond lengths and the splitting of the Si–Si PRDF first peak in high-pressure environments. In particular, the lengths of the edge- and face-sharing bonds correspond to the first sub-peak, whereas the length of corner-sharing bonds aligns with the second sub-peak. The slight deviation of the second sub-peak from the peak position associated with corner-sharing bond lengths is attributed to the superposition of bond length distributions among these three bond types.

Stishovite, a highly studied phase of silica, features a distinctive SiO_6 octahedral structure, setting it apart from other silica polymorphs with its denser silicon and oxygen atom arrangement [32]. This tetragonal structure is notable for its six-coordination of Si atoms [34], a contrast to the four-coordination observed in quartz and similar silica forms, presenting a more compact formation. In liquid SiO_2, the proportion of SiO_6 units significantly increases as pressure rises (see figure 2). The distribution of Si–O distances within SiO_6, shown in figure 5, centres around 1.69 Å. It is observed that with increasing pressure, the peak of the Si–O distance distribution becomes more pronounced. The Si–O bond lengths within SiO_6 at pressure in a range of 60–100 GPa are more stable than those at lower pressures, contributing to the formation of a more orderly stishovite crystal structure. The emergence of SiO_6 units plays a crucial role in the crystallisation of SiO_2 under compression, as evidenced in studies [45,46]. In [47], a SiO_2 glass sample is compressed across a range of 0–100 GPa [47]. The coordination number of Si in the glass transitions from 4 to 6 at pressures between 20 and 35 GPa, maintaining this six-fold coordination up to 100 GPa. This change aligns with observations of six-coordinated SiO_2 under

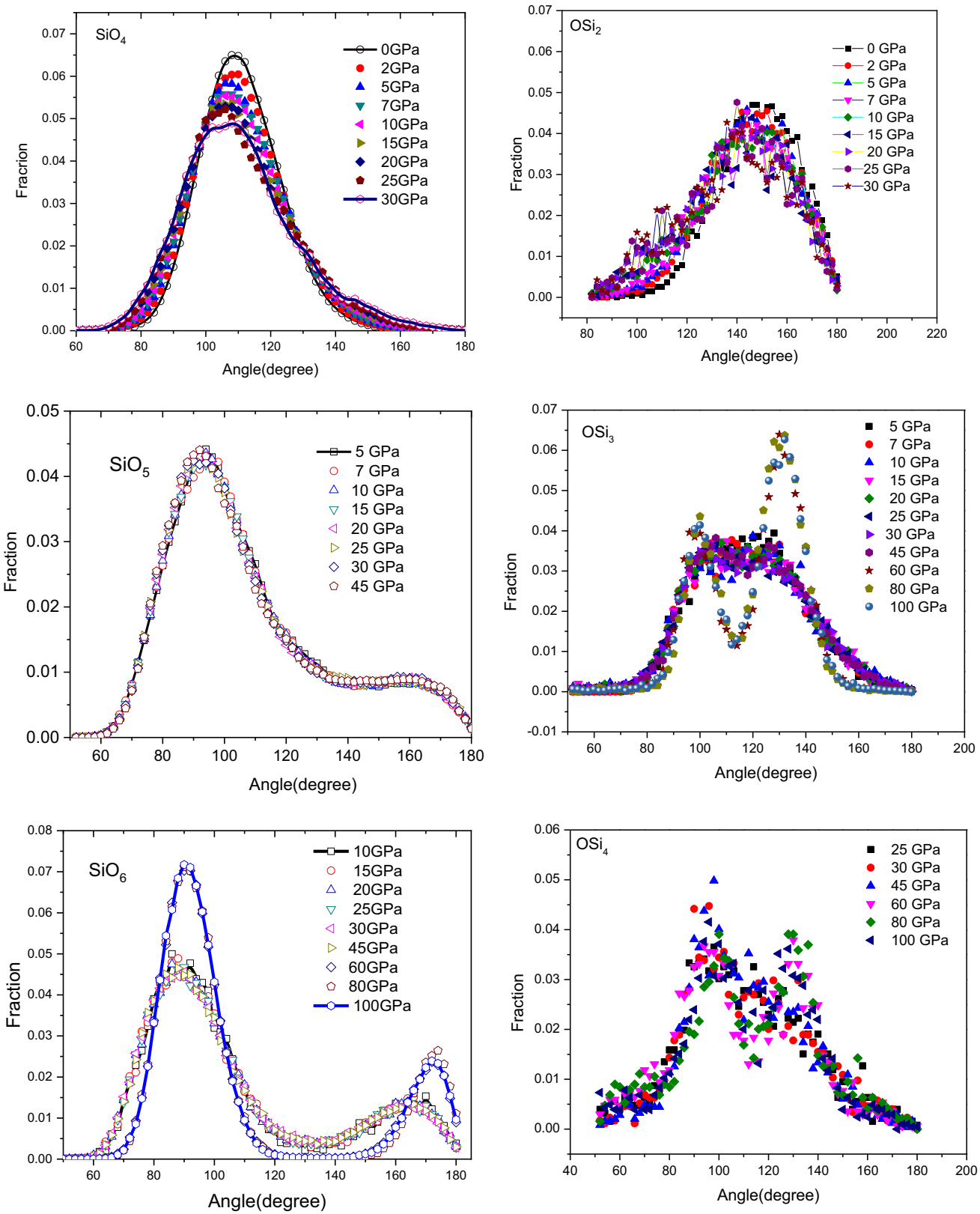

Figure 3. O–Si–O bond angle distributions in SiO_4, SiO_5 and SiO_6 units (*left*) and Si–O–Si bond angle distributions in OSi_2, OSi_3 and OSi_4 (*right*).

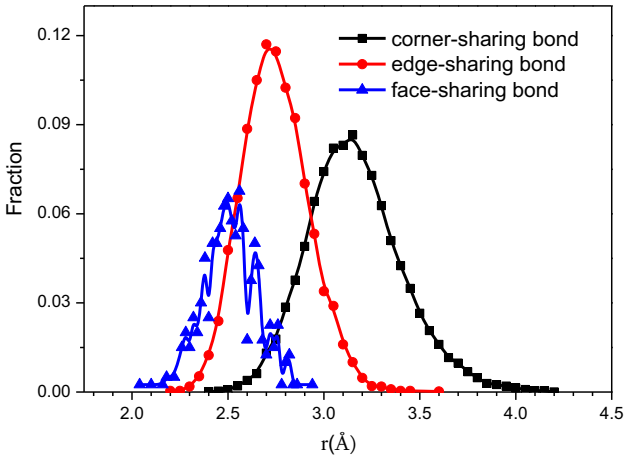

Figure 4. The average bond lengths of corner-, edge- and face-sharing bonds at 100 GPa.

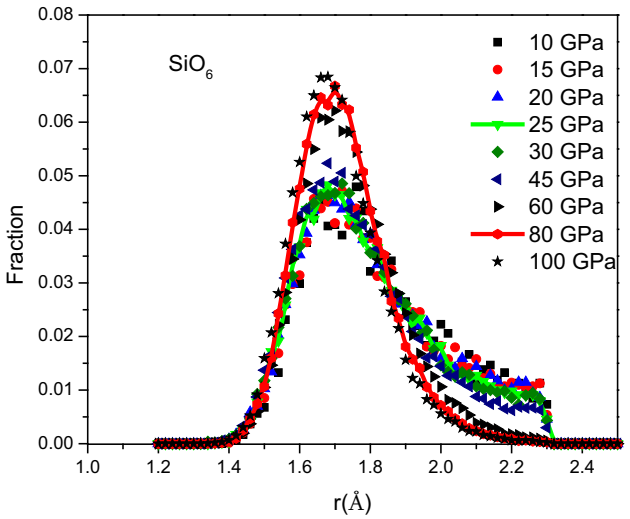

Figure 5. The Si–O distance distribution in SiO_6.

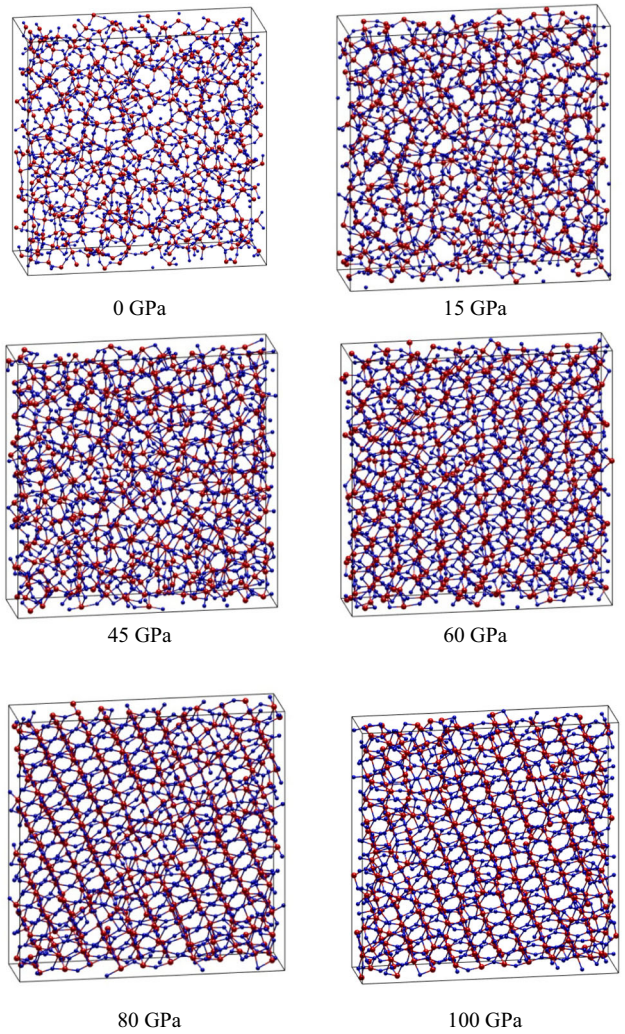

Figure 6. The –Si–O– network change under compression.

compression, suggesting that the stishovite crystallisation phase initiates at 35 GPa [48]. Notably, the Si–O distance in SiO_2 glass at this pressure is approximately 1.71 ± 0.2 Å, which is closely in agreement with the Si–O distance in SiO_6 units at 60 GPa of liquid SiO_2 in this study. Due to the higher pressure applied, the Si–O distances in SiO_6 units of liquid SiO_2 at the phase transition pressure are longer than those in glass SiO_2. Based on these observations, we propose that the initial liquid SiO_2 system transforms into a polymorphic state and subsequently transitions into a stishovite structure at 60 GPa.

Figure 6 shows the partial snapshot of the SiO_2 system under compression. In the range 0–45 GPa, the structure of the system appears disordered. However, a significant transformation is observed as the pressure increases from 60 to 100 GPa, where the system exhibits a marked increase in orderliness. This transition underscores the progression towards the crystalline formation, serving as a compelling piece of evidence that supports the emergence of a more structured and organised phase within the SiO_2 system under high-pressure conditions. This sequence of changes effectively illustrates the dramatic shift from a disordered to an ordered state, reinforcing the understanding of how pressure influences the structural dynamics and crystallisation process of SiO_2.

The distribution of SiO_x cluster sizes plays a pivotal role in the investigation of polymorphism within a given system [49,50]. Table 2 illustrates how the SiO_x cluster sizes vary across pressures ranging from 2 to 60 GPa. At 2 GPa, the majority of SiO_4 units are interconnected, forming a large cluster comprising 18,447 atoms, along four isolated SiO_4 units (five atoms each). The SiO_5 clusters are relatively smaller, with a maximum size of 100 atoms. Twenty-one isolated SiO_6 units are present at

Table 2. Distribution of SiO_x-cluster size at different pressures. N_{cl} is the number of clusters and N_{at} is the number of atoms per one cluster.

2 GPa		5 GPa		10 GPa		15 GPa		30 GPa		60 GPa	
N_{cl}	N_{at}	N_{cl}	N_{at}	N_{cl}	N_{at}	N_{cl}	N_{at}	N_{cl}	N_{at}	N_{cl}	N_{at}
Distribution of SiO_4 cluster size											
4	5	34	5–10	282	5–10	486	5–10	391	5–10	14	5
1	18,447	2	11–20	35	11–20	93	11–20	18	11–20		
		1	16,064	15	21–30	42	21–30	5	21–30		
				1	33	11	31–40				
				1	41	11	41–50				
				1	52	23	51–100				
				1	168	5	101–300				
				1	9537						
Distribution of SiO_5 cluster size											
269	6–10	181	6–10	49	6–10	13	6	32	6–10	115	6–10
89	11–20	72	11–20	8	11–20	1	11	7	11–20	31	11–20
26	21–30	21	21–30	2	31–40	1	14,398	1	13,328	2	21–30
15	31–40	13	31–40	1	12,417					2	41–50
8	41–50	4	41–50								
6	51–100	13	51–100								
		8	101–700								
		1	2678								
Distribution of SiO_6 cluster size											
21	7	116	7	231	7	165	7	16	7	1	19,718
		20	11–20	86	11–20	80	11–20	1	11		
		1	24	21	21–30	31	21–30	5	13		
				12	31–40	14	31–40	1	13,319		
				1	47	18	41–50				
				1	50	14	51–100				
				1	66	12	101–300				

2 GPa. With an increase in pressure, the large SiO_4 clusters fragment into smaller parts, leading to the formation of larger SiO_5 and SiO_6 clusters. The largest SiO_4 cluster diminishes significantly in size with increasing pressure, from 16,064 atoms at 5 GPa to just 30 atoms at 30 GPa. By 60 GPa, SiO_4 clusters are absent, leaving behind 14 isolated SiO_4 units. For SiO_5 clusters, the size peaks at 14,398 atoms at 15 GPa, indicating the highest relative fraction of SiO_5 in the system, as depicted in figure 2, before sharply declining to 50 atoms at 60 GPa. The maximum size of SiO_6 clusters shows a small increase at pressures up to 15 GPa. At 30 GPa, the largest SiO_5 cluster consists of 13,319 atoms. The pronounced change in the sizes of SiO_4, SiO_5 and SiO_6 units under pressures from 2 to 60 GPa and their non-uniform spatial distribution contribute to the system's polymorphism. Intriguingly, at 60 GPa, all the SiO_6 units are interconnected to form a single cluster, which supports the notion that the crystallisation process concludes at this pressure.

3.2 *Phase transition determined by density*

Liquid SiO_2 comprises two distinct states, or phases: a low-density phase and a high-density phase [51–53]. The low-density phase features a network structure primarily formed through OSi_2 linkages and the high-density phase features a network structure built around OSi_3 linkages. As pressure increases, there is a notable increase in OSi_3 linkages, leading to more

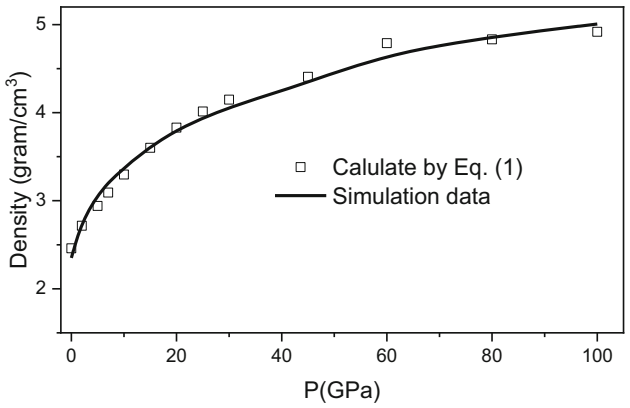

Figure 7. The density of SiO_2 is calculated based on (i) simulation data (size of simulation box and the number of atoms), (ii) eq. (1).

edge-shared links within the structure. This pressure-induced increase in edge-sharing linkages causes changes in the intermediate-range order (IRO) of the network structure of the liquid SiO_2.

In the regime of applied compressive forces, SiO_2 exhibits a continuous phase transition from a lower-density configuration predominated by OSi_2 linkages to a higher-density configuration predominated by OSi_3 linkages [15,54]. In the system, OSi_4 linkages account for a small percentage (see figure 2). Therefore, to simplify the calculation, we ignore the existence of OSi_4 linkages. Figure 7 shows the variation of the density of the model with pressures. The density of SiO_2 is about 2.4 g/cm^3 at 0 GPa and around 4.9 g/cm^3 at 100 GPa. In the previous work [55,56], for the melt SiO_2 at the temperature range 1900–2200 g/cm^3, the density of SiO_2, $\rho = 2.508 - 2.13 \times 10^{-4}$ T (g/cm^3), in which T is measured in Celsius. The structural constitution of liquid SiO_2 is an admixture of both low and high-density motifs within the interval. The density-specific structural networks are characterised by the predominance of either OSi_2 or OSi_3 linkages, with OSi_2 indicative of the low-density phase and OSi_3 of the high-density phase. The density (ρ) of the SiO_2 system at a given pressure is quantifiable via the ratio of OSi_2 and OSi_3 linkages as given in the following relation:

$$\rho_{\text{system}} = C_2\rho_L + C_3\rho_H, \tag{1}$$

where C_2 and C_3 represent the fractional presence of OSi_2 and OSi_3 linkages, respectively and ρ_L and ρ_H correspond to the densities intrinsic to the low- and high-density states [15]. The density of the system depends not only on the respective fraction of OSi_2 and OSi_3 but also on the arrangement of SiO_x ($x = 4, 5, 6$) basic units in the network [57]. The fit of the simulation data to eq. (1) is accurate, effectively capturing the phase transition of the system. The density of SiO_2 at 60 GPa is approximately 4.6 g/cm^3 in the simulation, closely aligned with a value of 4.7 g/cm^3 from the fitting data. These densities approach the value 4.9 g/cm^3 observed at 100 GPa, indicating the completion of the phase transition from polyamorphic to crystalline state at around 60 GPa.

3.3 *Ring statistics of the –Si–O– network*

To have a better understanding of the structural transformation of the –Si–O– network, we also analysed the ring statistics of the system under compression. The network is conceptualised as an undirected graph, with each atom representing a node. This framework allows for a detailed examination of the network's connectivity, identifying paths as sequences of nodes and bonds connected in succession without overlaps [44]. The study of rings within such networks utilises a variety of definitions [58–65], each offering a distinct perspective on the network's structure and properties. These methodologies differ in their approach to identifying and counting rings, which can lead to small variations in the calculated ring statistics. For this study, we employ the no-shortcut path criterion and its associated algorithm as introduced by Matsumoto *et al* [64]. This criterion is selected for its effectiveness in discerning ring structures within the –Si–O– network, defining an n-fold ring as a configuration consisting of nSi atoms and nO atoms. This methodological choice facilitates a targeted analysis of the network's ring structures, allowing for a deeper understanding of its geometric and physical characteristics. By adopting this approach, we contribute to a more comprehensive understanding of the network's structural intricacies.

Figure 8 presents an in-depth analysis of the Si–O ring statistics in liquid SiO_2 under compression, focussing on rings up to a maximum size of 12, comprising 24 atoms (12 oxygen and 12 silicon atoms). At ambient pressure, the predominance of sixfold rings is notably high. This observation is consistent with the findings in vitreous SiO_2 systems [63–66]. The predominance of the six-fold rings in both liquid and glass states can be attributed to the continuous random network structure formed by the fundamental SiO_4 tetrahedral units that characterise both the glass and liquid states of SiO_2. The distribution of Si–O ring sizes exhibits a Gaussian shape at ambient pressure, which is closely tied to the distribution of Si–O–Si and O–Si–O bond angles within the structure. These angles play a crucial role in the system's energy minimisation, influencing the overall shape of the ring statistics. The formation of twofold rings (or edge-sharing bonds) and threefold rings occurs through the shortening of the Si–Si distance, elongation of the Si–O bond and adjustments in the Si–O–Si and

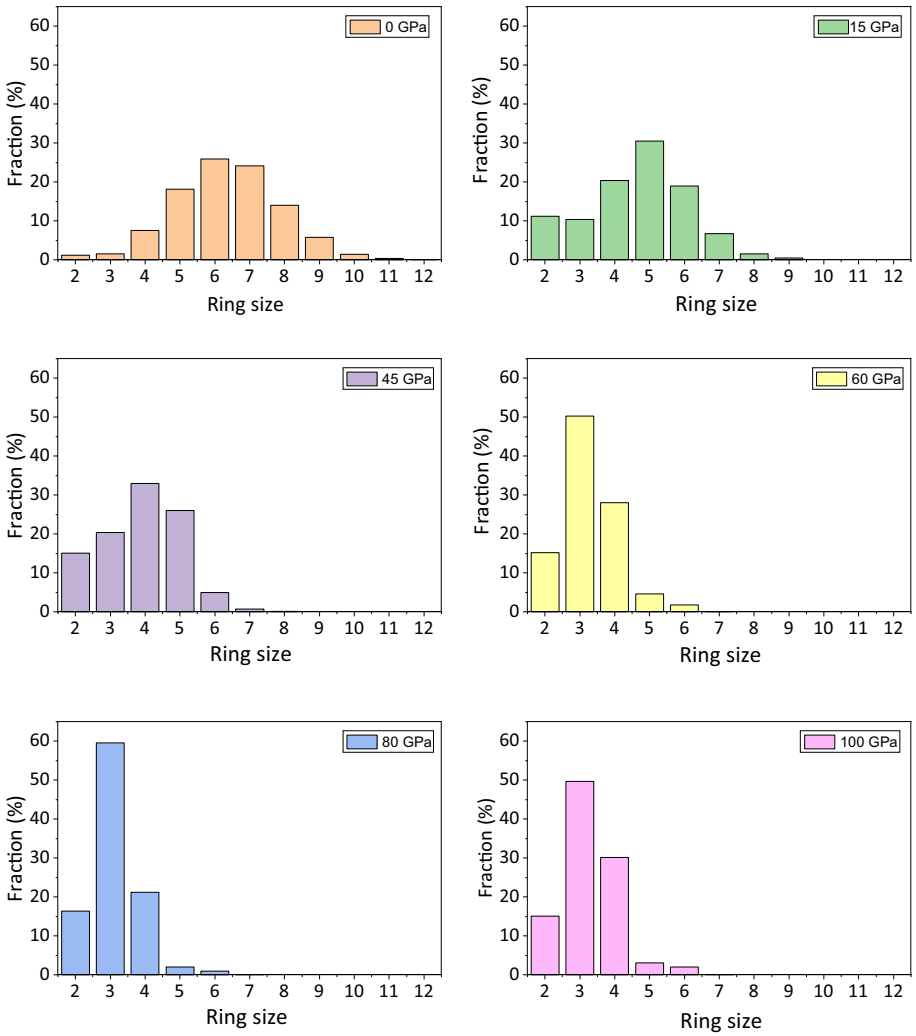

Figure 8. Si–O ring statistics under compression.

O–Si–O angles, aimed at reducing the system's energy. Consequently, these smaller rings represent only a minor fraction of the total. Larger rings, specifically those with 5, 6 and 7 members, display peak O–Si–O bond angle distributions approaching 109°, indicative of nearly perfect tetrahedral configurations. Therefore, the five-, six- and seven-fold rings have the highest distribution in the system [66]. As pressure escalates, the large rings break down into small rings. There is a marked increase in the number of edge-sharing linkages (see table 2), leading to a significant rise in the prevalence of twofold rings between 0 and 15 GPa. Between 15 and 45 GPa, fivefold rings become predominant, while threefold rings dominate the range 60–100 GPa, accounting for 50–60% of the observed structures. The maximum ring size decreases from 12-fold at 0 GPa to sixfold at pressures exceeding 60 GPa. The dramatic change in ring statistics, particularly between 45 and 60 GPa, underscores a strong structural phase transition from polyamorphism to the crystalline stishovite phase of the initial liquid SiO_2 model.

In the context of glass SiO_2, experimental data indicate a significant structural evolution with pressure, highlighted by the predicted and observed increases in the occurrence of two-, three- and four-fold rings [67,68]. Raman spectroscopy studies of glassy SiO_2 under pressures ranging from 8 to 30 GPa [68] signifies a notable shift in the structural topology of the material. Comparatively, in crystalline stishovite [69], the dominance of two-, three- and four-fold rings mirrors the Si–O ring statistics observed in the high-pressure liquid SiO_2 system of this study. From this comprehensive analysis, we deduce a crystallisation process occurring between 45 and 60 GPa, marking a transition from polyamorphism to the crystalline structure of stishovite in the initial liquid SiO_2 model, thus highlighting a critical pathway in the understanding of SiO_2's behaviour under extreme conditions.

4. Conclusion

This study advances our understanding of the structural transformations and crystallisation mechanisms in liquid SiO_2 under high-pressure conditions. Significant insights have been obtained by closely examining the local –Si–O– network structure and IRO through MDS. The investigation reveals a complex transition from polyamorphic liquid SiO_2 to crystalline stishovite, highlighted by the evolution of Si–O, O–O and Si–Si PRDFs under varying pressures. Notably, the structural transformation is most apparent in the pressure range of 5–60 GPa, where the system transitions through phases characterised by SiO_4, SiO_5 and SiO_6 units, eventually stabilising in an octahedral network indicative of stishovite formation beyond 60 GPa. The analysis of bond lengths, bond angles and coordination numbers under compression sheds light on the underlying mechanisms of silica's phase transition. The emergence of SiO_6 units and the corresponding changes in the Si–O–Si and O–Si–O bond angle distributions provide comprehensive evidence of silica's transition towards a more ordered and crystalline phase under high pressure. The ring statistics of SiO_2 under compression reveal a clear transition in the structural configuration of –Si–O– network, emphasising the dominance of sixfold rings at ambient pressure due to the continuous random network formed by SiO_4 tetrahedral units. Upon compression, a notable shift towards fivefold rings up to 15 GPa and subsequently threefold rings dominating at pressure from 60 to 100 GPa, indicates a significant structural phase transition. This shift is especially pronounced between 45 and 60 GPa, marking the transition from polyamorphism to a crystalline stishovite phase. The polyamorphic state of liquid SiO_2 is analysed by the formation of SiO_x clusters at a pressure below 60 GPa. Experimental data further support this crystallisation process, highlighting a crucial understanding of behaviour of SiO_2 liquid under extreme pressure conditions. This insight into the pressure-driven structural phase transitions provides a deeper comprehension of the crystallisation dynamics and the intricate behaviour of liquid SiO_2. MDS and explorer discover analysis in this work can be applied to other glassy oxide systems such as germania and glassy silicate systems.

Acknowledgements

The simulation was conducted using the high-performance computing system at RIKEN. Representative laboratory at RIKEN: RIKEN Cluster for Pioneering Research, Theoretical Quantum Physics Laboratory and RIKEN Center for Computational Science, Discrete Event Simulation Research Team.

References

[1] D I Grimley, A C Wright and R N Sinclair, *J. Non-Cryst. Solids* **119**, 49 (1990)
[2] A Takada, P Richet, C R A Catlow and G D Price, *J. Non-Cryst. Solids* **345–346**, 224 (2004)
[3] C Zhang and K Najafi, *J. Micromech. Microeng.* **14**, 769 (2004)
[4] A Ashok and P Pal, *Sci. World J*. **2014** (2014). https://doi.org/10.1149/2.01715022jss
[5] T Tsuchiya and J Tsuchiya, *Proc. Natl. Acad. Sci.* **108**, 1252 (2011)
[6] J Sarnthein, A Pasquarello and R Car, *Phys. Rev. B* **52**, 12690 (1995)
[7] A N Payzullaev *et al*, *ECS Adv*. **2**, 031001 (2023)
[8] A J Gratz, L D DeLoach, T M Clough and W J Nellis, *Science* **259**, 663 (1993)
[9] L Huang, M Durandurdu and J Kieffer, *Nat. Mater*. **5**, 977 (2006)
[10] X Zhang *et al*, *J. Chem. Phys*. **157**, 134703 (2022)
[11] L T San, N V Hong and P K Hung, *High Press. Res*. **36**, 187 (2016)
[12] A Takada, P Richet, C R A Catlow and G D Price, *J. Non-Cryst. Solids* **353**, 1892 (2007)
[13] P K Hung and N V Hong, *Eur. Phys. J. B* **71**, 105 (2009)
[14] V P Prakapenka, G Shen, L S Dubrovinsky, M L Rivers and S R Sutton, *J. Phys. Chem. Solids* **65**, 1537 (2004)
[15] V Van Hoang, *Phys. Lett. Sect. A Gen. At. Solid State Phys*. **335**, 439 (2005)
[16] L Huang, J Nicholas, J Kieffer and J Bass, *J. Phys. Condens. Matter* **20**, 075107 (2008)
[17] P F McMillan *et al*, *J. Phys. Condens. Matter* **19**, 415101 (2007)
[18] G Sfuncia *et al*, *Cryst. Eng. Comm.* **25**, 5810 (2023)
[19] M A Machado Filho *et al*, *Cryst. Growth Des.* **24**, 4717 (2024)
[20] M Zuo *et al*, *ACS Appl. Eng. Mater.* **1**, 1229 (2024)
[21] Y Daia and M Song, *Mater. Res*. **22**, 5 (2019)
[22] B B Karki, D Bhattarai and L Stixrude, *Phys. Rev. B* **76**, 104205 (2007)
[23] B B Karki, D Bhattarai, M Mookherjee and L Stixrude, *Phys. Chem. Miner*. **37**, 103 (2010)
[24] A Saksaengwijit and A Heuer, *J. Phys. Condens. Matter* **19**, (2007)
[25] P K Hung, N V Hong and L T Vinh, *J. Phys. Condens. Matter* **19**, 466103 (2007)
[26] B W H van Beest, G J Kramer and R A van Santen, *Phys. Rev. Lett*. **64**, 1955 (1990)
[27] Y Wang *et al*, *Nat. Commun*. **5**, 1 (2014)
[28] Q Mei, C J Benmore and J K R Weber, *Phys. Rev. Lett*. **98(5)**, 057802 (2007)
[29] B B Karki, *Theor. Comput. Meth. Miner. Phys. Geophys. Appl*. **71**, 355 (2018)
[30] Y Waseda and J M Toguri, *Metall. Trans. B* **8**, 563 (1977)

[31] D Andrault, R J Angle, J L Mosenfelder and T Le Bihan, *Am. Mineral*. **88**, 301 (2003)
[32] K J Kingma, R E Cohen, R J Hemley and H-K Mao, *Lett. to Nat*. **374**, 243 (1995)
[33] D Andrault, G Fiquet, F Guyot and M Hanfland, *Science* **282**, 720 (1998)
[34] D C Palmer, R J Hemley and C T Prewitt, *Phys. Chem. Miner*. **21**, 481 (1994)
[35] F Mauri, A Pasquarello, B G Pfrommer, Y G Yoon and S G Louie, *Phys. Rev. B: Condens. Matter Mater. Phys.* **62**, R4786 (2000)
[36] R L Mozzi and B E Warren, *J. Appl. Crystallogr*. **2**, 164 (1969)
[37] P G Coombs *et al*, *Philos. Mag. B Phys. Condens. Matter; Stat. Mech. Electron. Opt. Magn. Prop*. **51**, 39 (1985)
[38] J Neuefeind and K D Liss, *Phys. Chem. Chem. Phys*. **100**, 1341 (1996)
[39] R F Pettifer, R Dupree, I Farnan and U Sternberg, *J. Non-Cryst. Solids* **106**, 408 (1988)
[40] V V Le and G T Nguyen, *J. Non-Cryst. Solids* **505**, 225 (2019)
[41] N M Anh, N T T Trang, T T Nguyet, N Van Linh and N Van Hong, *Comput. Mater. Sci*. **177**, 109597 (2020)
[42] N H Son, N H Anh, P H Kien, T Iitaka and N Van Hong, *Model. Simul. Mater. Sci. Eng*. **28**, (2020)
[43] N Hoang Anh, N H Son and N Van Hong, *VNU J. Sci. Math.- Phys.* **39**, 53 (2023)
[44] H A Nguyen and N Van Hong, *Phys. Scr*. **98**, 045919 (2023)
[45] T Sato and N Funamori, *Phys. Rev. Lett.* **101**, 255502 (2008)
[46] P Dera, J D Lazarz, V B Prakapenka, M Barkley and R T Downs, *Phys. Chem. Miner*. **38**, 517 (2011)
[47] C Meade, R J Hemley and H K Mao, *Phys. Rev. Lett*. **69**, 1387 (1992)
[48] T Sato and N Funamori, *Phys. Rev. B: Condens. Matter Mater. Phys.* **82**, 1 (2010)
[49] M T Lan, T T Duong, N V Huy and N Van Hong, *Mater. Res. Express* **4(3)**, 035202 (2017)
[50] L T San, N Van Hong, T Iitaka and P K Hung, *Eur. Phys. J. B* **89**, 1 (2016)
[51] T Morishita, *Phys. Rev. Lett*. **93**, 055503 (2004)
[52] D Daisenberger *et al*, *Phys. Rev. B: Condens. Matter Mater. Phys*. **75**, 224118 (2007)
[53] E Lascaris, M Hemmati, S V Buldyrev, H E Stanley and C A Angell, *J. Chem. Phys*. **142**, 104506 (2015)
[54] P K Hung, N V Hong, G T T Trang and T Iitaka, *Mater. Res. Express* **6**, 085201 (2019)
[55] I A Aksay and J A Pask, *J. Am. Ceram. Soc.* **62**, 332 (1979)
[56] J F Bacon, A A Hasapis and J W W Jr, *Phys. Chem. Glas*. **1**, 90 (1960)
[57] P Koziatek, J L Barrat and D Rodney, *J. Non-Cryst. Solids* **414**, 7 (2015)
[58] X Yuan and A N Cormack, *Comput. Mater. Sci*. **24**, 343 (2002)
[59] F Wooten, *Acta Crystallogr. Sect. A Found. Crystallogr*. **58**, 346 (2002)
[60] D S Franzblau, *Phys. Rev. B* **44**, 4925 (1991)
[61] K Goetzke and H J Klein, *J. Non-Cryst. Solids* **127**, 215 (1991)
[62] S V King, *Nature* **213**, 1112 (1967)
[63] S Le Roux and P Jund, *Comput. Mater. Sci*. **49**, 70 (2010)
[64] M Matsumoto, A Baba and I Ohmine, *J. Chem. Phys*. **127**, 134504 (2007)
[65] T Taniguchi, M Okuno and T Matsumoto, *J. Non-Cryst. Solids* **211**, 56 (1997)
[66] R K Kalia, A Nakano and P Vashishta, *Phys. Rev. B* **47**, 3053 (1993)
[67] K Trachenko, M T Dove, V V Brazhkin and J C Phillips, *J. Phys. Condens. Matter* **15**, (2003)
[68] R J Hemley, H K Mao, P M Bell and B O Mysen, *Phys. Rev. Lett*. **57**, 747 (1986)
[69] C J Benmore *et al*, *Phys. Rev. B: Condens. Matter Mater. Phys*. **81**, 1 (2010)